High-performance water gas shift induced by asymmetric oxygen vacancies: Gold clusters supported by ceria-praseodymia mixed oxides

Junjie Shi [a,b,*,1], Hailian Li [a,1], Alexander Genest [c,1], Weixuan Zhao [a], Pengfei Qi [d], Tao Wang [a], Günther Rupprechter [c,**]

[a] School of Chemistry & Chemical Engineering, Yantai University, Yantai 264005, China
[b] Department of Chemical Engineering, University of Florida, Gainesville, FL 32611, United States
[c] Institute of Materials Chemistry, TU Wien, Getreidemarkt 9/BC, A-1060 Vienna, Austria
[d] State Key Laboratory of Bio-Fiber and Eco-textiles, College of Materials Science and Engineering, Collaborative Innovation Center for Marine Biobased Fibers and Ecological Textiles, Institute of Marine Biobased Materials, Qingdao University, No. 308 Ningxia Road, Qingdao 266071, China

ARTICLE INFO

ABSTRACT

Modifying and controlling sites at the metal/oxide interface is an effective way of tuning catalytic activity, beneficial for bifunctional catalysis by reducible oxide supported metal nanoparticles. We employed mixed ceria-praseodymia supported Au clusters for the water gas shift reaction (WGSR). Varying the Ce: Pr ratio (4:1, 2:1, 1:4) not only allows to control the number of oxygen vacancies but, even more important, their local coordination, with asymmetrically coordinated O# being most active for water activation. These effects have been examined by X-ray absorption near edge structure (XANES), extended X-ray absorption fine structure (EXAFS), X-ray photoelectron spectroscopy (XPS), Raman spectroscopy, temperature programmed desorption/reduction (TPD/TPR), and density functional theory (DFT). Using the WGSR performance of Au/CeO_x as reference, $Au/Ce_4Pr_1O_x$ was identified to exhibit the highest activity, with a CO conversion of 75% at 300°, which is about 5-times that of Au/CeO_x. $Au/Ce_4Pr_1O_x$ also showed excellent stability, with the conversion still being 70% after 50 h time-on-stream at 300°. Although a higher Pr content leads to more O vacancies, the catalytic activity showed a "volcano behavior". Based on DFT, this was rationalized via the formation energy of oxygen vacancies, the binding energy of water, and the asymmetry of the O# site. The presented route of creating active vacancy sites should also be relevant for other heterogeneous catalytic systems.

1. Introduction

Mixed oxides are widely used in many industrial processes, including chemical manufacturing, energy conversion, and environmental protection. They have received much attention in heterogeneous catalysis due to their superior performance in many redox reactions, such as CO oxidation, water-gas shift reaction (WGSR), and soot combustion, and as active supports for metal nanoparticles [1–3].

The excellent performance of mixed oxides is typically attributed to their reducibility (oxygen vacancy formation) and sites at the oxide/metal interface [4–7]. For example, Si et al. reported that both model $CeO_x/TiO_2(110)$ and powder CeO_x/TiO_2 supported Au catalysts exhibit better WGSR activity than either of the individual oxide counterparts

[8]. This is due to a higher oxygen vacancy concentration in CeO_x/TiO_2, which facilitates the limiting step of WGSR, i.e., H_2O dissociation. Many studies thus focused on increasing the oxygen vacancy content, e.g., by doping metal ions with different valence states into the oxide, which creates oxygen vacancies due to charge compensation [2,9–11].

However, increasing the concentration of oxygen vacancy (defect) sites does not increase the catalytic performance in a simple monotonous relationship. For example, increasing the Mn^{2+} doping of CeO_2 increased the number of vacancies, but the CO oxidation rate first increased (up to $Ce_{0.92}Mn_{0.08}O_{2-\delta}$), but then decreased (up to $Ce_{0.82}Mn_{0.18}O_{2-\delta}$) [12,13]. A similar trend was reported for Bi-doped CeO_2 by Zhou et al. with $Ce_{0.8}Bi_{0.2}O_{2-\delta}$ exhibiting the best performance, whereas higher doping ($Ce_{0.7}Bi_{0.3}O_{2-\delta}$ and $Ce_{0.5}Bi_{0.5}O_{2-\delta}$)

---

significantly lowered activity [13]. Apparently, the effect of defect sites (O vacancies, metastable cations) in mixed oxides does not merely depend on their concentration, but seems also related to the chemical environment of the active sites (lattice distortion, site symmetry, interaction between defects etc.) [13–15]. In fact, using scanning tunneling microscopy (STM), Esch et al. directly revealed different O vacancy structures (dimer, trimer, linear cluster) on single crystal $CeO_2(111)$ [16]. Complementing studies by density functional theory (DFT) suggested that their activities in chemical reactions were also different [17].

Deposited noble metal nanoparticles such as Cu, Au, or Pt can also enhance the oxide support reducibility [9,18]. In fact, the interaction of metal nanoparticles with oxide supports has been intensely studied for decades, and two well-known explanations have been proposed: the Mars-van Krevelen (M-vK) mechanism and strong metal-support interaction (SMSI) [18–25]. The first is often used to rationalize why reducible oxides promote CO oxidation on metal catalysts, as lattice oxygen of the reducible support is directly involved in the reaction via the metal-oxide interface [26]. The second effect is related to metal-promoted support reduction, i.e., the initial states of encapsulation may enhance activity. Inspired by these two principles, metal-support interactions have been intensively studied for reducible oxides [1,10,11,27–32].

However, the specific interactions of *mixed oxides* and supported metals were only rarely examined in detail [1,2,11,28,29]. It is also unclear how the interaction of two metastable cations may change the chemical symmetry in mixed oxides, thus affecting the active sites, even more so in the case of bifunctional catalysis involving metal clusters/nanoparticles. We have systematically studied these interactions for ceria-praseodymia mixed oxide supported Au. With Ce and Pr being neighbors in the periodic table, some properties of ceria and praseodymium oxide are similar [33–35]. Both contain "switchable" tri- and tetravalent cations, creating the ability to remove/uptake lattice oxygen [35,36]. Indeed, praseodymia was reported to exhibit the most O vacancies of all rare-earth oxides [34–36]. Furthermore, Ce and Pr cations of the same valence have similar radii ($Ce^{4+} = 1.110$ Å; $Pr^{4+} = 1.100$ Å; $Ce^{3+} = 1.283$ Å; $Pr^{3+} = 1.266$ Å), facilitating to mix them in one oxide matrix [35]. Pr-doped ceria has shown promising applications for soot, CO, and particulate matter oxidation, as well as the Prins-condensation-hydrolysis reaction [37–44]. Still, applications of ceria-praseodymia supported Au have been rarely reported.

Moreover, WGSR is known as important step for industrial generation and purification of H_2 [33,34,45–52]. Recently, it has gained impact for eliminating CO and simultaneously producing hydrogen for proton-exchange membrane fuel cells (PEMFCs), especially since Flytzani-Stephanopoulos and others reported gold/oxide catalysts with exceptional WGSR performance at relatively low temperature (200–300 °C) [47].

Along these lines, we used WGSR for benchmarking the activity of various $Au/Ce_aPr_bO_x$, with the goal to rationalize the effects of composition on the catalyst surface structure, and thus on the nature of the active sites in a relatively complex system. It has been suggested that adjusting the Ce:Pr cation ratio not only changes the abundance of oxygen vacancies, but also modifies the symmetry of the Pr-O-Ce bond [35], which may play a key role in H_2O dissociation in WGSR. According to Zhou and co-workers, the formation of "asymmetric oxygen vacancies" in mixed oxides makes oxygen "easy come, easy go", accounting for their enhanced activity in redox reactions [13]. Nevertheless, more detailed insight including modeling is clearly needed for a thorough understanding of this concept.

Apparently, using well-defined catalyst is equally important. We employed a hydrothermal synthesis for preparing cerium-praseodymium mixed hydroxide, with Au loaded by a modified deposition–precipitation method. Based on recent work [34], the hydroxide can be directly used as a support, yielding gold with small size and high dispersion. The abundant hydroxyl groups act as strong anchoring sites for the Au complexes in solution and allow the stabilization of small gold

clusters, but not of larger gold particles. The catalytic activity of $Au/Ce_aPr_bO_x$ towards WGSR was studied in a plug-flow reactor. High-resolution transmission electron microscopy (HRTEM), high-angle annular dark-field imaging (HAADF) and energy-dispersive X-ray fluorescence (EDX) elemental mapping were employed for structure analysis. In order to examine interactions between metal and support, as well as between metal cations within the oxide, X-ray absorption near edge structure (XANES), extended X-ray absorption fine structure (EXAFS), X-ray photoelectron spectroscopy (XPS), Raman, and temperature programmed desorption/reduction (TPD/TPR) were carried out. Density functional theory (DFT) modeling of various mixed oxide compositions was used to evaluate the oxygen vacancy formation energy, the water binding energy, and the asymmetry of specific O vacancy sites. Altogether, this enabled us to explain the origin of the Pr concentration (doping) effect on catalytic performance and to single out the crucial role of asymmetric vacancy sites in the rate-determining step of H_2O dissociation.

2. Experimental and Modeling

2.1. Catalyst preparation

Different Ce:Pr ratios in Ce-Pr(OH)$_x$ were prepared via a hydrothermal method. First, the designated amount of $Pr(NO_3)_3$ (0.25 mol/L, purity 99.5%, Meryer chemical technology Co.) solution was added drop-wise to NaOH solution (6 M; purity 99.5%, Guoyao company) under stirring for 15 mins, followed by adding $Ce(NO_3)_3$ solution (0.25 mol/L; purity 99.5%, Meryer chemical technology Co.) drop-wise to the above formed suspension, with the mixture subsequently kept at room-temperature under stirring for 1 h to ensure homogeneity, before being tightly sealed in a polytetrafluoroethylene (PTFE) lined stainless-steel autoclave. The total amount of $Pr(NO_3)_3$ and $Ce(NO_3)_3$ was kept at 3.75 mmol, the molar ratio of Ce:Pr was controlled by adjusting the amount of $Ce(NO_3)_3$ and $Pr(NO_3)_3$. The sample composition is termed as $Ce_aPr_bO_x$, with a/b being the Ce to Pr molar ratio. Following hydrothermal treatment at 100 °C for 24 h, the precipitate was collected and washed with deionized (DI) water. In order to exclude an effect of residual Na ions, the precipitate was thoroughly washed (at least 10 times) with repeated ultrasonic dispersion and centrifugal separation, until the supernatant had a pH close to 7. The sample was dried overnight at 60–90 °C to obtain the $Ce_aPr_b(OH)_x$ support.

Au was loaded on $Ce_aPr_b(OH)_x$ through a modified deposition-precipitation (MDP) method, as reported previously [34]. Typically, 0.3 g of $Ce_aPr_b(OH)_x$ powder was added to 10 mL of $HAuCl_4$ and KOH mixed solution with pH around 9 (yielding a nominal Au loading of 1 wt %). After aging at room temperature for 1 h, adding 20 mL ammonia and aging for another 2 h, the suspension was filtered and washed with DI water several times, until no Cl$^-$ was detected anymore (with $AgNO_3$ solution), then dried at 60–100 °C overnight without any heat treatment afterwards. The obtained samples were denoted as $Au/Ce_aPr_b(OH)_x$. It has been reported that chloride has a great affinity to oxides, inducing metal sintering and oxide aggregation [53–55]. However, in our study we did not observe Au sintering or pronounced loss of oxide surface area, excluding an effect of Cl$^-$ trace amounts.

2.2. Catalyst characterization

Inductively coupled plasma optical emission spectrometry (ICP-OES, Leeman Labs Inc.) was applied to determine the exact gold loading of the catalysts. N_2 adsorption-desorption measurements were carried out on a Micromeritics ASAP2020HD. Prior to the experiments, the samples were degassed at 200 °C for 3 h and nitrogen adsorption was performed at −203 °C. The Brunauer-Emmett-Teller method was used to calculate the surface area, pore volume, and average pore size of each sample. X-ray diffraction (XRD) patterns were obtained on a Rigaku SmartLab III diffractometer using Cu Kα radiation (λ = 1.5406 Å, 30 mA, 40 kV) with

a scanning rate of 10 ° min^{-1} in 2θ range from 10 °− 80 °. X-ray photoelectron spectroscopy (XPS) analysis of metal oxidation states and atomic ratios of the surface region of the gold/ceria-praseodymia mixed oxide catalysts was performed on an Axis Ultra XPS spectrometer (Kratos, U.K.), using a monochromatized Al Kα (225 W) radiation source and a 165 mm mean radius hemispherical analyzer (overall yielding a resolution of 0.1 eV; binding energies calibrated via the C 1 s peak at 284.5 eV). XPS measurements were carried out at room temperature without sample pre-treatment.

Transmission electron microscopy (TEM), high-resolution TEM (HRTEM) and high-angle annular dark-field scanning transmission electron microscopy (HAADF-STEM) were performed on a JEOL JEM-3010 microscope equipped with a Cs-corrector for the objective lens, with the imaging system operated at 200 kV. EDS spectral imaging was carried out with the Gatan Microscopy Suite. The spatial resolution of the STEM/EDS measurement depends on the number of pixels per scanned region. For the measurements shown below the spatial resolution was between 0.5 and 3 nm. The Au LIII-edge X-ray absorption fine structure (XAFS) spectra were measured at BL14B2, SPring-8 (Hyogo, Japan) [56]. Raman spectra were recorded on a confocal Raman microscope (senterra II spectrometer, BRUKER) using a 532 nm laser under ambient conditions, for a scanning range of 50–2000 cm^{-1} and a resolution of 1 cm^{-1}.

The pulsed CO chemisorption, O$_2$ temperature-programmed desorption (O$_2$-TPD), CO-TPD, and H$_2$ temperature-programmed reduction (H$_2$-TPR), were acquired on a Micromeritics AutoChem II 2920. Prior to measurements, all samples were first exposed to reaction conditions (2 vol% CO, 10 vol% H$_2$O at 300 °C) for 2 h to stabilize their chemical state. Pulsed CO chemisorption was used to determine the Au dispersion (measured CO flow rate 1.338 mmol/min, sample mass 0.1 g), with the samples pretreated in Ar stream at 200 °C for 60 min to remove adsorbates and monitored through cooling to room temperature in Ar. For O$_2$-TPD, samples were first purged in He for (2 h, 200 °C), after that cooled to 50 °C and treated in 10% O$_2$/He for 1 h. The analysis was carried out in He (50 mL/min) from 50° to 850 °C with a heating rate of 10 °C /min. For CO-TPD, samples were purged in He (50 mL/min, 1 h, 50 °C), then exposed to 10% CO/He (50 mL/min, 1 h, 50 °C). After purging with He for 40 min, the analysis was carried out in He (30 mL/min) from 50° to 800 °C (heating rate of 5 °C/min) monitoring masses 44 and 28 by mass spectrometry. For H$_2$-TPR, samples were purged in He (50 mL/min, 1 h, 200 °C), after that treated in 20% O$_2$/He for 30 min at 350 °C, then cooled to 25 °C and then exposed to 10% H$_2$/He for ~ 30 min until the base line was stable. The analysis was carried out in 10% H$_2$/He, 50 mL/min from 50° to 850°C with a rate of 10 °C/min. Most characterizations were done for the active catalysts after 10 h on stream (note the induction period of ~2.5 h), to reflect the properties of active catalysts under steady-state conditions. According to McFarland and Metiu, heterogeneous catalytic reactions run under steady-state (non-equilibrium) conditions that cannot be accurately described by property parameters of as-prepared catalysts, which are more likely in thermodynamic equilibrium during preparation [10].

2.3. Catalytic activity tests

The catalytic performance in WGSR was determined in a continuous flow reactor at atmospheric pressure. The reactor was a U-shaped glass tube with an inner diameter of 10 mm and a thermocouple placed near the outer surface of the catalyst bed. The powder samples (45 mg) were placed between two quartz wool plugs in the middle of the tube. Cerium-praseodymium hydroxide supported Au was used in the as-prepared form after drying without any further pre-treatment (reduction or calcinations), as it undergoes self-activation under reaction conditions. For the water gas shift measurements, the reaction gases consisted of a mixture of CO (2 vol%), H$_2$O (10 vol%), N$_2$ as carrier gas, and a total flow of 45 mL/min. The gas composition was set by mass flow controllers (Seven-star, China), with the water vapor adjusted via a

temperature-controlled saturator (H$_2$O vapor pressure at 42 °C: 1×10^4 Pa; ~10 vol%) and dosed through a heated pipe (100 °C). An ice condenser was used to remove water from the reactor exit gas stream. All feed components and products were analyzed by an online Agilent 7890 gas chromatograph (GC) equipped with a molecular sieve column and a thermal conductivity detector (TCD). The gas composition was sampled every 30 °C after maintaining each temperature for 30 min to obtain representative catalyst performance. The kinetic studies were carried out in the same reactor and by changing the amount of catalysts the conversion rate was kept below 20%. For every test at least two cycles (150–400 °C) were carried out to get reliable conversion rates. In the 2nd cycle (Fig. S1), the catalytic activity was only ~ 5% lower. Long-term stability tests were performed at 300 °C under the same conditions (CO 2 vol%, H$_2$O 10 vol%, N$_2$ as carrier gas, total flow 45 mL/min, m$_{catalyst}$ 50 or 100 mg). The conversion of CO was quantified by the area normalization method and calculated by the following formula:

$$X_{CO} = (CO_{in} - CO_{out} / CO_{in}) * 100\%$$

The turnover frequencies (TOF), were calculated based on metal dispersion, following the equation:

$$TOF \ (s^{-1}) = (X_{CO}/100) * F_{CO} * (M_{Au}/(W_{cat} * X_{Au} * D_{Au}))$$

with X_{CO} being the CO conversion at a certain temperature, F_{CO} the flow rate of CO (mol/s), M_{Au} the molar weight of Au (196.96 g/mol), W_{cat} the catalyst weight, X_{Au} the Au loading, and D_{Au} the dispersion of Au.

2.4. Modeling by DFT

DFT calculations using the PBE+U formalism were carried out as implemented in the Vienna Ab initio Simulation Package, VASP [57–59]. The target was to rationalize experiments over various Ce$_a$Pr$_b$O$_x$ model structures using the (111) surface. The projector augmented wave formalism was applied using a cutoff energy of 400 eV [60,61]. We used U = 5 eV for both, the Ce and the Pr 4 f orbitals. In view of the size of the slab model with 10 Å vacuum spacing we carried out the Brillouin-zone integration using a 3×3×1 k-point mesh. The focus was set on rationalizing chemical effects rather than intrinsic materials properties. This means we explored selected distributions of reduced centers, M^{3+}, focused on a standard anti-ferromagnetic coupling of all spins, and on adsorption processes at specific positions. Based on the calculated unit cell of CeO$_2$, we devised a 2 × 2 surface model using 4 layers, with centers in the "bottom" 2 layers fixed at their calculated bulk position. Geometry optimizations were considered converged when the atomic force dropped below 0.02 eV/Å. The unit cell of CeO$_2$ contains 4 metal centers, which were gradually replaced by Pr to model the substitution of Pr into CeO$_2$, following an arbitrary order. To indicate the degree of substitution we use the ratio Pr to Ce b:a in the unit cell.

To form an oxygen vacancy, we removed a neutral O moiety, leaving 2 reducing electrons in the system, which we placed always at two metal centers at the same position. For b > 0 these positions were occupied by Pr. We kept the U values equal for Ce and Pr, not to bias the tendency of reduction between Ce and Pr. CO was adsorbed at Ce and Pr sites. The vacancy formation energy E$_v$ and the other binding energies were calculated according to

$$E_v = E(MO_2 - O) − E(MO_2) − 0{\cdot}5E(O_2)$$

$$E_{CO} = E(CO@MO_2) − E(MO_2) − E(CO)$$

$$E_{H2O} = E(H_2O@MO_2 - O) − E(MO_2 - O) − E(H_2O)$$

meaning that negative values indicate a favorable formation. This is analogous for E$_{CO}$. For E$_{H2O}$ we chose the system with a vacancy as reference, as this is likely the surface on which water adsorbs for activation.

3. Results and discussion

3.1. Structural and morphological studies

The X-ray diffraction patterns of cerium-praseodymium mixed hydroxide ($Au/Ce_aPr_b(OH)_x$) and pure cerium hydroxide supported Au catalyst ($Au/Ce(OH)_x$) are shown in Fig. S2. Before WGSR $Au/Ce(OH)_x$ and $Au/Ce_aPr_b(OH)_x$ show the hexagonal structure of $Ce(OH)_3$ (JCPDS 74–0665) or $Pr(OH)_3$ (JCPDS 83–2304) due to the similar ionic radius of Ce^{3+} (0.128 nm) and Pr^{3+} (0.126 nm) [34,62,63]. After WGSR ($\sim$ 10 h), the XRD patterns are obviously different, with $Au/Ce_4Pr_1O_x$ and $Au/Ce_2Pr_1O_x$ showing diffraction peaks similar to those of Au/CeO_x, corresponding to a face-centered cubic structure (JCPDS 04–059) [63]. All peak positions of the Pr doped samples are slightly shifted to lower 2θ angles, which can be attributed to a lattice expansion caused by replacing Ce^{4+} (1.110 Å) by larger Pr^{3+} (1.266 Å). This confirms that Pr has been successfully inserted into the ceria lattice [35,38]. Broader reflections of $Au/Ce_1Pr_4O_x$ indicate smaller ceria-praseodymia crystallites than in the other samples [64]. No distinct peaks of gold particles were observed for all samples, demonstrating the high Au dispersion. The XRD results indicate that the catalyst supports restructured during WGSR.

The bulk and surface composition of different catalysts were determined by ICP-OES and XPS, respectively. The bulk Au concentration (ICP) on the $Ce_aPr_bO_x$ supports varies from 0.62 wt% to 0.82 wt% (Table S1), which is close to the intended value (1 wt%), confirming the effectiveness of depositing dispersed Au on the hydroxide surface. The amount of surface Au measured by XPS was around 0.36–0.41 atom% for all three samples. BET (Table S1) indicated specific surface areas (SSA) in the range of 51–73 m^2 g^{-1}(gold loading did basically not negatively affect the textural properties), which was maintained during reaction.

The shapes and exposed facets of the $Au/Ce_aPr_bO_x$ catalysts were examined by TEM and HRTEM. The exemplary (HR)TEM images of $Au/Ce_4Pr_1O_x$ in Fig. 1 show that after WGSR (150–400 °C, 10 h) the support exhibits rod-shape with a mean diameter around 10–15 nm and a length of 80–150 nm, demonstrating that no agglomeration or sintering occurred upon reaction. The Ce:Pr ratio has almost no effect on the diameter and length of the nanorods (Fig. S3). The HRTEM images in Fig. 1b, c show interplanar spacings of 0.27 nm corresponding to the {200} plane of CeO_2. The interplanar spacing of 0.32 nm corresponds to both {111} planes from CeO_2 or Pr_6O_{11}, and their solid solutions, as both exhibit similar distances [34,62,63,68]. High densities of atomic steps, kinks and dislocations are also evident (Fig. 1b, c), characteristic for all $Ce_aPr_bO_x$ supports, which were likely caused by mixing Ce-Pr (with slightly different ionic radii) in the same matrix. It is known that under-coordinated surface sites in the form of steps, kinks and dislocations have a high surface energy, which can be active sites for adsorbing H_2O and CO, accounting for the high WGSR reactivity.

In Fig. 1d the protruding feature shows a lattice spacing of 0.23 nm corresponding to the (111) plane of Au, indicative of a Au cluster with ~1.3 nm diameter. However, such small gold clusters were rarely detected by HRTEM, and only a thin edge parts of the support, suggesting that most of Au was well dispersed on the support either as nanoclusters (< 1.5 nm) or even as single atoms. Apparently, this prevented the determination of a mean Au particle size. This holds true for all catalysts, as Au was very well dispersed in all of them. The result is quite similar to the study from Si et al., who reported that on the ceria surface no noticeable gold nanoparticles were found on rod-shaped and polyhedral CeO_2 support [65].

A representative HAADF-STEM image in Fig. 1e shows bright areas (circled by white dotted lines) with diameters smaller than 1.5 nm that originate from Au. In HAADF-STM (z-contrast imaging), the Au atoms appear brighter than the lighter Ce and Pr. This was further confirmed by the elemental map of Au in Fig. 1f, which corresponds well to the HAADF-STEM (apart from the very small cluster). The total number of detected Au clusters was still too small to provide a meaningful mean Au cluster size. Moreover, the EDX maps of Ce (Fig. 1g) and Pr (Fig. 1h) illustrate their high and homogeneous elemental distribution. The above analysis clearly confirms highly dispersed and small sized Au clusters on the $Ce_4Pr_1O_x$ support. This likely originates from the hydroxyl groups and O vacancies (confirmed by XPS, Raman) on the support, acting as strong anchoring sites for the Au complexes during deposition-precipitation, allowing the stabilization of gold clusters, but not of larger gold particles (which are formed in the case of pure CeO_2) [66,67,69].

3.2. Catalytic performance

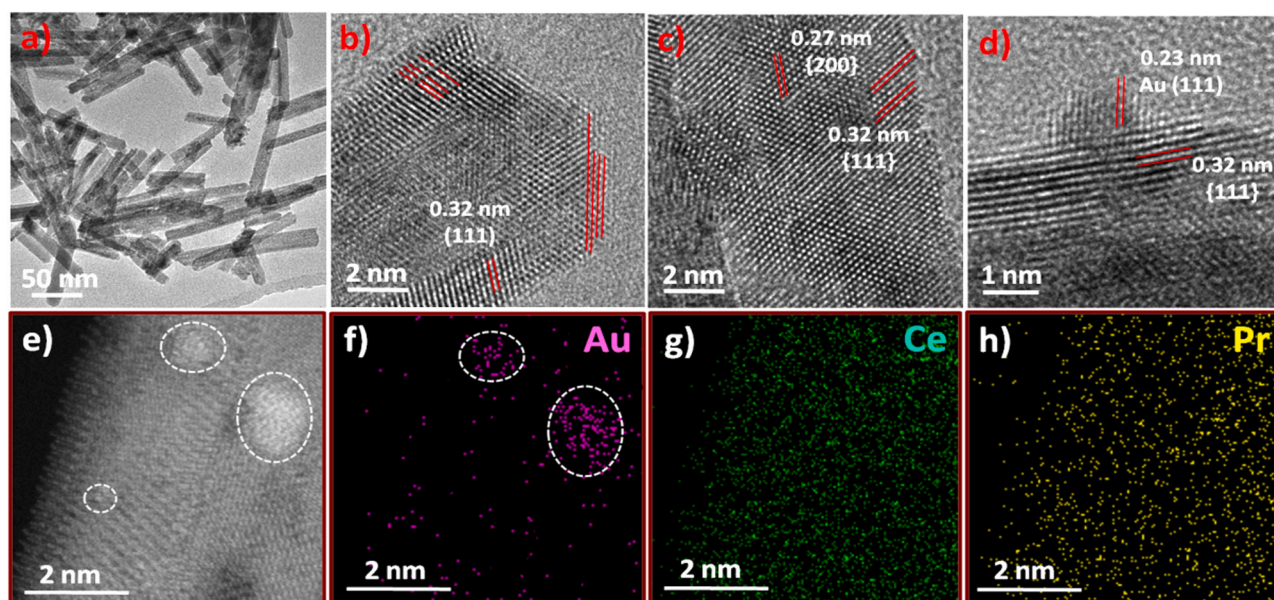The catalytic WGSR performance of $Au/Ce_aPr_bO_x$, Au/CeO_x and Au/

Fig. 1. (a) TEM, (b, c, d) HRTEM and (e) HAADF-STEM micrographs of $Au/Ce_4Pr_1O_x$; (f, g, h) Elemental distribution maps with Au (pink), Ce (green), Pr (yellow). Images acquired after 10 h WGSR from 150 °C to 400 °C.

PrO_x was investigated in a continuous flow reactor (pure $Ce_aPr_bO_x$, CeO_x and PrO_x were almost inactive with CO conversion < 4% even at 400 °C). Fig. 2a shows the steady-state activity profiles of the catalysts. In the entire temperature range (150–400 °C), the praseodymia containing samples exhibit much higher activity than Au/CeO_x and Au/PrO_x, in the order of: $Au/Ce_4Pr_1O_x$ > $Au/Ce_2Pr_1O_x$ > $Au/Ce_1Pr_4O_x$ > Au/CeO_X > Au/PrO_x. At 300 °C, the CO conversion over $Au/Ce_4Pr_1O_x$ reached 75%, which is about 2.5 times that of Au/CeO_x, 3.75 times that of Au/PrO_x, 1.2 times that of $Au/Ce_2Pr_1O_x$ and 1.7 times that of $Au/Ce_1Pr_4O_x$. The turnover-frequencies (TOFs) at 360 °C were calculated by assuming that all surface Au atoms were active sites (Au dispersion measured by pulsed CO chemisorption). The bar graphs in Fig. 2b display the TOFs of all five catalysts: $Au/Ce_4Pr_1O_x$ ($2.0\ s^{-1}$) > $Au/Ce_2Pr_1O_x$ ($1.2\ s^{-1}$) > $Au/Ce_1Pr_4O_x$ ($0.6\ s^{-1}$) > Au/PrO_x ($0.5\ s^{-1}$) > Au/CeO_x ($0.4\ s^{-1}$). The TOF of $Au/Ce_4Pr_1O_x$ is even higher than that reported by Fu et al. for Au/CeO_2 ($1.27\ s^{-1}$, at 350 °C) and that reported by Liu et al. for $Au@TiO_{2-x}/ZnO$ ($0.49\ s^{-1}$, at 325 °C) [31,47]. The different behavior of the catalysts suggests that the nature of the support plays a key role in determining the catalytic activity, because the Au loading/dispersion is very similar in all cases. Still, the high activity of $Au/Ce_aPr_bO_x$ must originate from a synergistic effect of Au species and the $Ce_aPr_bO_x$ support [64].

The measured apparent activation energies (E_a, Fig. 2c) amount to 27.3, 26.5, 27.1, 30.4 and 21.5 kJ mol^{-1} for $Au/Ce_4Pr_1O_x$, $Au/Ce_2Pr_1O_x$, $Au/Ce_1Pr_4O_x$, Au/CeO_x and Au/PrO_x, respectively. Despite the differences of the WGSR rates over the $Au/Ce_aPr_bO_x$ and Au/CeO_x catalysts, the apparent activation energies were somewhat similar (26–30 kJ mol^{-1}). This suggests the same reaction mechanism for all and that the small difference in E_a must originate from the different nature of active sites. The lower E_a on $Au/Ce_aPr_bO_x$ (26–27 kJ mol^{-1}) as compared to Au/CeO_x (30 kJ mol^{-1}) highlights the benefits of using $Ce_aPr_bO_x$ mixed oxide supports. Although Au/PrO_x showed the lowest activation energy (21.5 kJ mol^{-1}), its conversion and rate were actually low, Fig. 2c. A small activation energy is generally expected to lead to a higher reaction rate constant, but according to the Arrhenius equation that also depends on the pre-exponential factor (frequency factor). The observation of low reaction rates despite small activation energies has also been reported for other catalysts, e.g. [70,71]. Nevertheless, the current apparent activation energies are comparable to those reported by Fu et al. and Si et al., who measured an E_a of 37 kJ mol^{-1} on Au/CeO_2 and 32 kJ mol^{-1} on $Au/(Ti-Ce)O_2$ mixed oxides [8,47].

One of the major obstacles in practical applications of Au-based catalysts is rapid deactivation, caused by accumulation of intermediates on the active sites (poisoning by carbonates/formates) and/ or agglomeration of Au species [33,45,72,73]. We thus tested the stability of $Au/Ce_4Pr_1O_x$ for WGSR at 300 °C under steady state conditions.

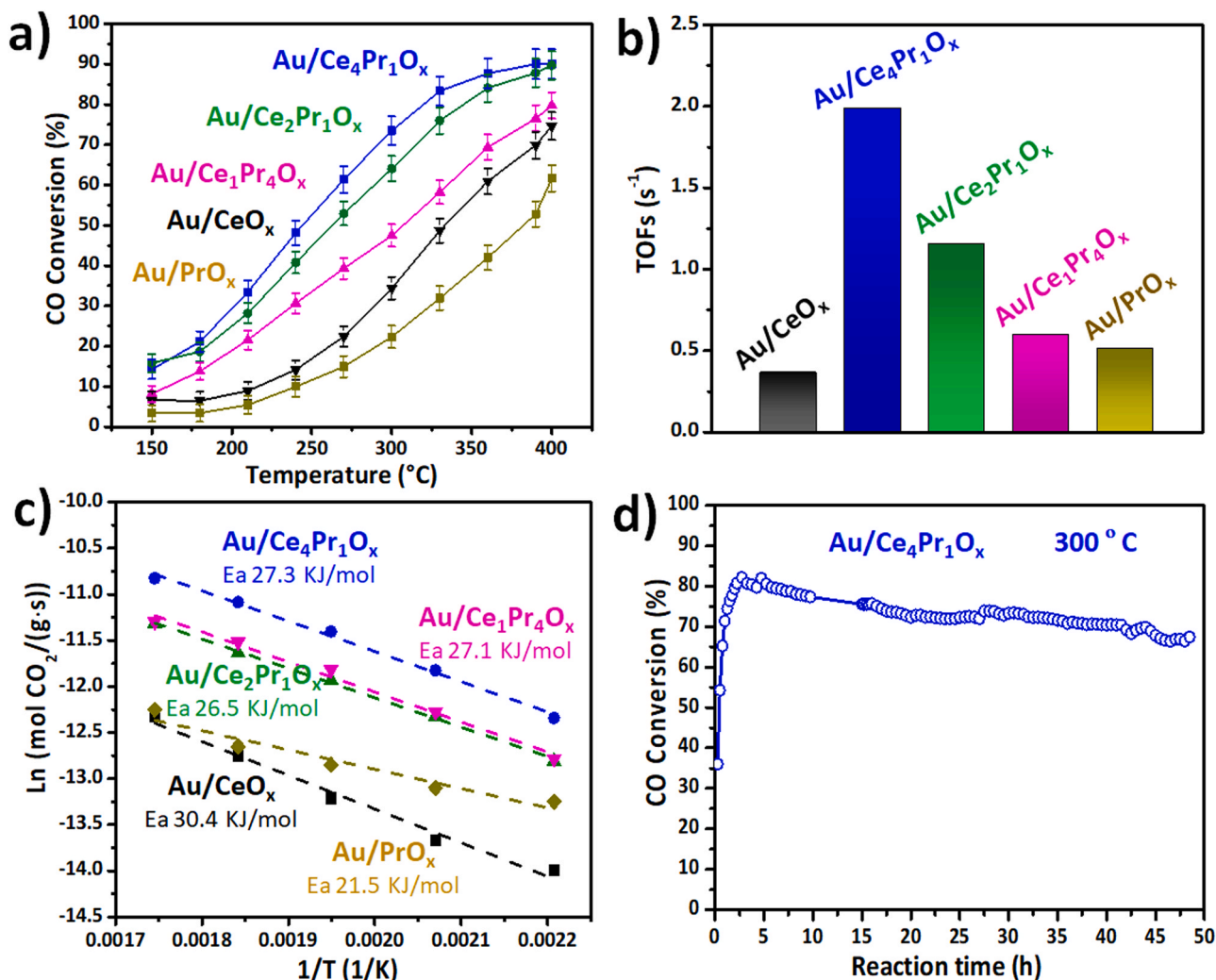**Fig. 2.** a) Steady-state temperature profiles of $Au/Ce_aPr_bO_x$, Au/CeO_x and Au/PrO_x catalysts for the WGS reaction (conditions: 2 vol% CO/10 vol% H_2O/N_2, 45 mL/ min, m_{catal} = 50 mg, space velocity 54,000 mL $h^{-1}g_{cat}^{-1}$); b) Histogram of TOF values of WGSR at 360 °C for $Au/Ce_aPr_bO_x$, Au/CeO_x and Au/PrO_x; c) Arrhenius plots of WGS over $Au/Ce_aPr_bO_x$ and Au/CeO_x. The space velocity of 270000 mL $h^{-1}g_{cat}^{-1}$ used was much higher than that in steady-state to ensure reaction within the kinetic regime (conversion of CO < 20%); d) Long-term stability test at 300 °C for $Au/Ce_4Pr_1O_x$ (reaction conditions as in steady-state).

As shown in Fig. 2d, after 50 h continued time-on-stream the conversion only decreased from 82% to 75%. In addition, by increasing the amount of catalyst to 100 mg and reducing the space velocity, the CO conversion rate at 300 °C was close to 100%, and there was almost no decrease in catalytic activity for up to 18 h (Fig. S4). To the best of our knowledge, the Au/Ce₄Pr₁Oₓ catalyst is among the most stable catalysts reported so far. For example, in a study of Jia et al., even at lower T (250 °C) the reactivity of ceria supported Au clusters decreased from 83% to 59% within 50 h [45].

3.3. Investigation of electronic metal-support interaction

X-ray absorption fine structure (XAFS) and X-ray photoelectron spectroscopy (XPS) were used to examine electronic interactions between Au and the $Ce_aPr_bO_x$ supports. The XANES spectra of Au L3 edges correspond to the 2p-5d electronic transition, the position and intensity of which are closely related to the 5d electronic structure and oxidation state [8,74,75]. As shown in Fig. 3a, the Au^{3+} (from Au_2O_3) XANES spectra exhibit a sharp and narrow absorption white line at around 11920 eV, which corresponds to the transition of electrons from the $2p_{3/2}$ core level to the vacant $5d_{3/2}$ and $5d_{5/2}$ [56,74,75]. The XANES spectra of Au/Ce₄Pr₁Oₓ and Au/Ce₂Pr₁Oₓ are similar to that of the Au foil, displaying almost no white line and indicating that most Au is

metallic (Au^0) after WGSR, due to the completely filled 5d state [56,75]. However, close inspection shows that the Au/Ce₄Pr₁Oₓ spectra (Fig. 3a inset) are not fully coinciding with that of Au foil. The slight broadening in the band of 11948 eV suggests that additional interactions between Au and the oxide support exist. The corresponding EXAFS data after Fourier transform (FT) in R-space are shown in Fig. 3b. The two peaks around 2.5 and 3.2 Å for Au/Ce₄Pr₁Oₓ and Au/Ce₂Pr₁Oₓ can be attributed to a single Au-Au shell, the splitting is due to Ramsauer-Townsend resonance [45,74,75]. The relatively low intensity in the Au-Au shell compared to that of Au foil indicates the formation of small Au nano-clusters. This is in line with the HRTEM observation and EDX mapping. Moreover, a weak shell at ~1 Å (Au-O) can be identified both for Au/Ce₄Pr₁Oₓ and Au/Ce₂Pr₁Oₓ, which is due to Au bonding to the support. The Au-Au interaction (2.5 Å) on Au/Ce₂Pr₁Oₓ is slightly weaker, while the Au-O band (1.0 Å) is stronger. This indicates that gold seems "more oxidized" in Ce₂Pr₁Oₓ than in Ce₄Pr₁Oₓ.

The XPS in Fig. 3c shows the deconvoluted spectra of Au 4 f using a Gaussian peak fitting method. Two major peaks at 83.9 and 87.7 eV, that can be assigned to Au^0, represent over 85% on all three samples (Au/Ce₄Pr₁Oₓ, Au/Ce₂Pr₁Oₓ and Au/Ce₁Pr₄Oₓ) after WGSR (Fig. S5). The binding energy at 85.4 eV is assigned to Au^{1+} and the two bands at 87.2 and 89.9 eV are assigned to Au^{3+} [34,76,77]. The total amount of ionic Au only slightly increased with increasing Pr concentration. The high
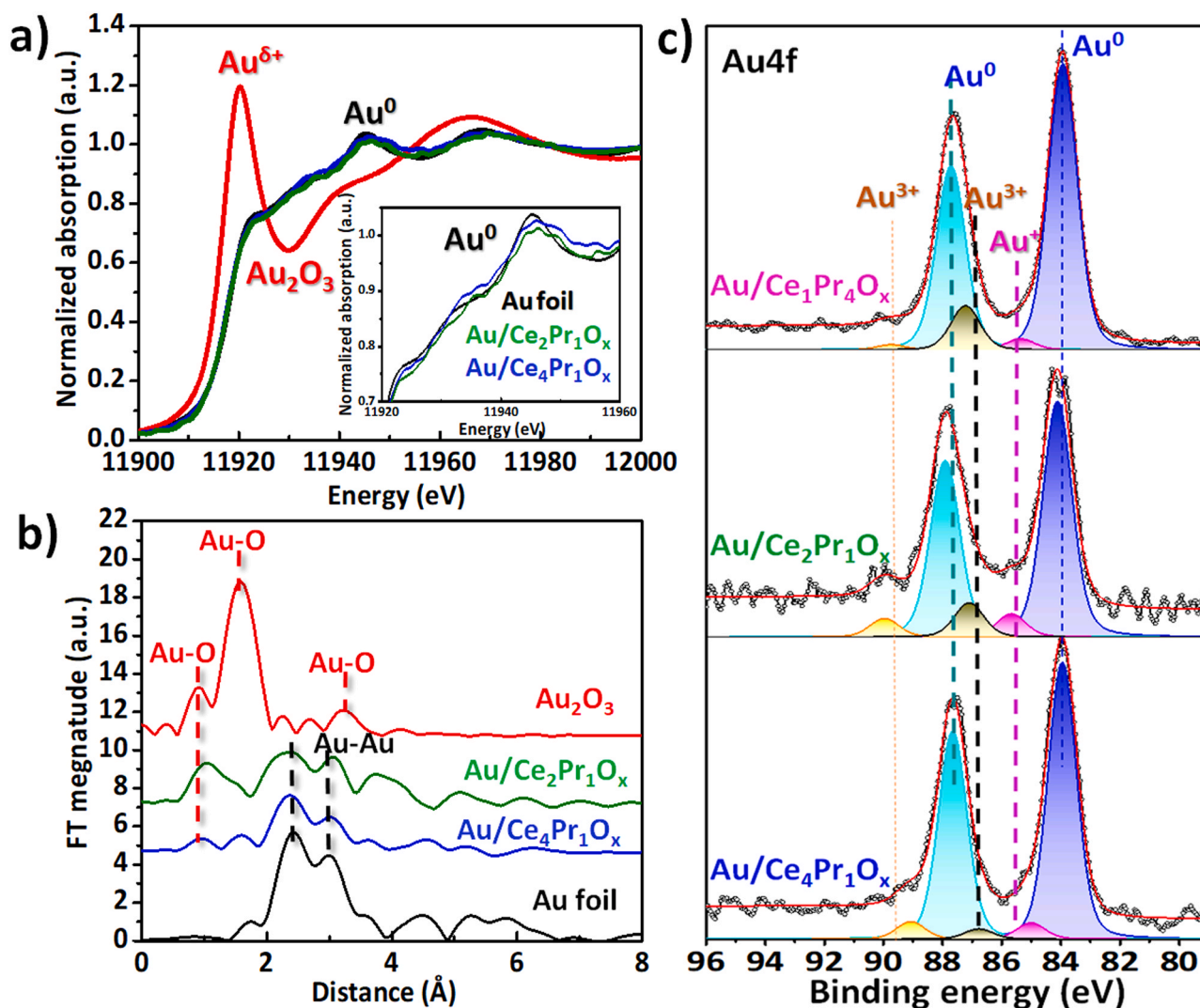

Fig. 3. a) Au LIII-edge X-ray absorption near-edge structure (XANES) spectra (the inset shows an enlarged range), b) Au LIII-edge extended X-ray absorption fine structure (EXAFS) fit and c) Au4f XPS spectra of Au/$Ce_aPr_bO_x$ catalysts after WGSR (2 vol% CO + 10 vol% H_2O/N_2, 10 h on-stream, 150–400ºC).

amounts of Au^0 after reaction are probably due to the strongly reducing atmosphere of WGSR, which agrees with the findings of Si et al. and Jia et al. [8,45] The positively charged Au and Au-O band, corroborated by EXAFS and XPS, confirm the electron transfer from Au to the $Ce_aPr_bO_x$ support [8,45]. It has been intensively disputed whether metallic gold or ionic gold create an active site in water gas shift. Based on the current work, this cannot be answered. Still, we demonstrate that by changing the oxide composition one can also affect the extent of ionic gold, providing a route to favorably modify the active sites.

To further investigate the chemical nature of the oxide support, particularly of electronic interactions between Ce and Pr, we explored the valence states of both Ce and Pr. The Ce $3d_{3/2}$ spectra of the three $Au/Ce_aPr_bO_x$ catalysts are displayed in Fig. 4a, suggesting that the majority of cerium species is in Ce^{4+} oxidation state, and partially as Ce^{3+} in different samples. Fig. 4b displays the corresponding Pr 3d XPS spectra. Due to the hybridization of 4 f^2 and 4 f^3L (L hole) and the multiple coupling of unpaired 4 f electrons with the 3d hole, the analysis of the Pr3d spectra is complex, but Schaefer et al. [78] conducted systematic studies on praseodymium oxides under UHV conditions. They assigned the peak at 977 eV (Fig. 4b) to an O KLL Auger emission, while peaks centered at 973 and 949 eV (Fig. 4b) are related to the oxidation degree of praseodymium oxide [35,78–80]. The intensities of these two peaks can therefore be used as indicators of the Pr^{4+}content. In turn, the two peaks at 953 and 956 eV, due to a hybridization of O 2p and Pr 4 f, are attributed to Pr^{3+} [34,78].

Fig. 4c illustrates changes of Ce^{3+}, Pr^{3+} and Pr^{4+} concentrations, given as ratios. The approximation of the Ce^{3+}, Pr^{3+} and Pr^{4+} content was obtained by calculating the percentage of XPS peak areas of Ce^{3+}, Pr^{3+} and Pr^{4+} relative to the total areas. The sample with the lowest Pr content ($Au/Ce_4Pr_1O_x$) showed the highest ratio of Ce^{3+} and Pr^{4+}, which is in line with results from Niu et al. ($Ce_{0.8}Pr_{0.2}O_{2-\delta}$ contained the highest Ce^{3+} ratio) [35]. Evidently, the Ce^{3+} and Pr^{4+} ratios decreased (Fig. 4c) with higher Pr content, whereas Pr^{3+} increased. This can be explained by the redox potential of Ce^{4+}/Ce^{3+} (1.7 V) which is lower than that of Pr^{4+}/Pr^{3+} (3.2 V), favoring Pr^{3+} [81].

Moreover, the chemical environment, particularly the symmetry of the chemical bonds, may also play a key role, as discussed in more detail below. When Ce is surrounded by symmetric Pr-O bonds (such as Pr-O-Ce-O-Pr or Pr_2-O-Ce-O-Pr_2), the electronic forces may cancel each other. In a recent review paper, Zhou and co-workers suggested asymmetric M-

O-$(Ce)_3$ sites as intrinsically active sites in redox reactions [13].

3.4. O vacancy studies

XPS and Raman spectroscopy, the latter being highly sensitive to oxygen displacement, were employed to examine the surface and bulk oxygen vacancies, induced by mixing Ce and Pr. Under the current conditions, XPS probes a sampling depth of several nm (depending on the inelastic-mean-free-path (IMFP) of photoelectrons of specific kinetic energy), while Raman (532 nm laser) penetrates 0.6–1.5 μm [82–84]. Complementing XPS characterization of *surface* O vacancies, Raman was applied to characterize the abundance of *bulk* oxygen vacancies.

The O 1 s spectra in Fig. 5a display 3 peaks, with the binding energy of around 529 eV characterizing lattice oxygen of Ce^{4+}-O_2 and Pr^{4+}-O_2. (cf. Fig. S6) [85,86]. Features near 531.0 eV originate from Ce^{3+}-OH or Pr^{3+}-OH, i.e., the reactant water dissociated on O vacancies (O #). As these species indicate the abundance of O#, they have also been labelled O_v in the literature [85–87]. Xu et al. used in situ DRIFTS to study H_2O dissociation on O vacancy rich Ni@TiO_{2-x}, detecting Ti^{3+}-OH which indicated that $O_v−Ti^{3+}$ directly participated in H_2O dissociation [32]. In the current case, for the higher Pr amounts, the 531.0 eV peak mostly originates from Pr^{3+}-OH (cf. Fig. 4). The third peak at 531.5 eV is assigned to adsorbed (molecular) water (surface hydroxyl-like groups) [85].

The Raman spectra in Fig. 5b of all samples show a strong band at around 460 cm^{-1}, which is attributed to the F_{2g} vibration mode of fluorite-type ceria, corresponding to the wagging vibration of an O atom between two Ce^{4+} ions [83,88,89]. Obviously, the peak intensity in the range of 540–630 cm^{-1} (Fig. 5b) increased with the ratio of Pr in oxide supports, which is in line with the results of Wang et al. [38] However, the interpretation of these bands is still controversially discussed: Sartoretti et al. assigned the peak at 550–570 cm^{-1} to oxygen vacancies coupled to the presence of Ce^{3+} or other cations; the peak at 600 cm^{-1} is an "intrinsic" O vacancy site already present in pure ceria, known as Frenkel defects; the peak at around 620 cm^{-1} is disorder-associated and linked to "extrinsic" defects, generated by dopants [89]. Based on a theoretical study, Teng et al. ascribed the peaks at 560 cm^{-1} and 600 cm^{-1} to the stretching vibration of O between M^{3+} and Ce^{4+} ions, near oxygen defects and without oxygen defects, respectively [84].

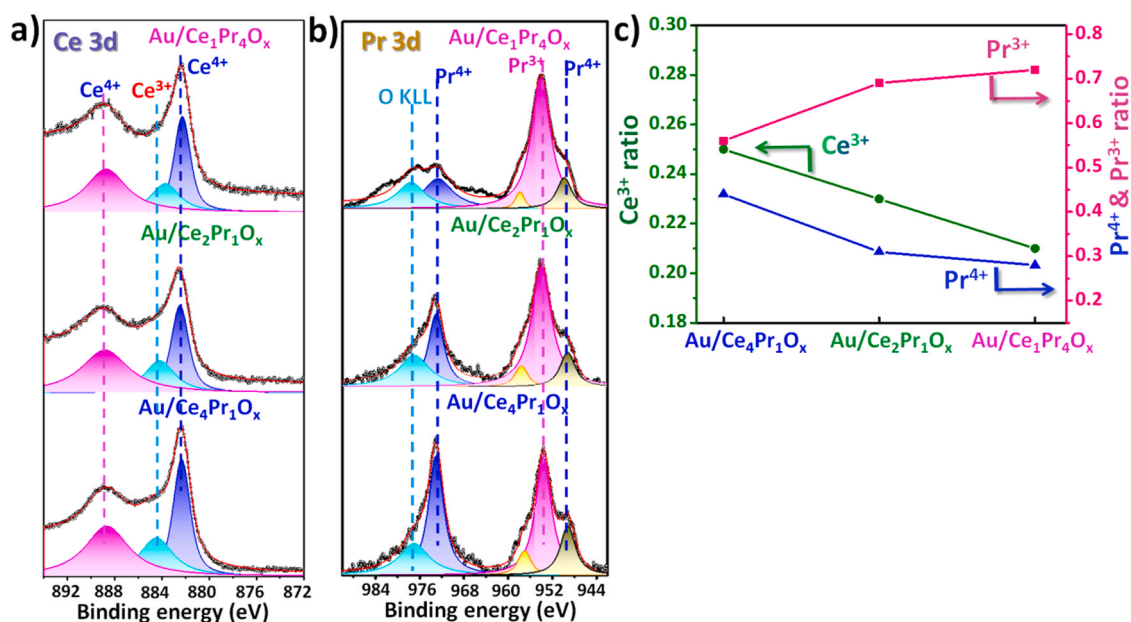In Fig. 5c, the ratio of surface (from XPS) and bulk (from Raman)

Fig. 4. Photoemission (XPS) spectra of (a) Ce 3d and (b) Pr 3d of $Au/Ce_aPr_bO_x$ catalysts after WGSR (2 vol% CO + 10 vol% H_2O/N_2, 10 h on-stream, 150–400°C); (c) Plots of Ce^{3+}, Pr^{3+} and Pr^{4+} ratio (peak area of Ce^{3+}/ or Pr^{3+}/ or Pr^{4+}/total peak area).
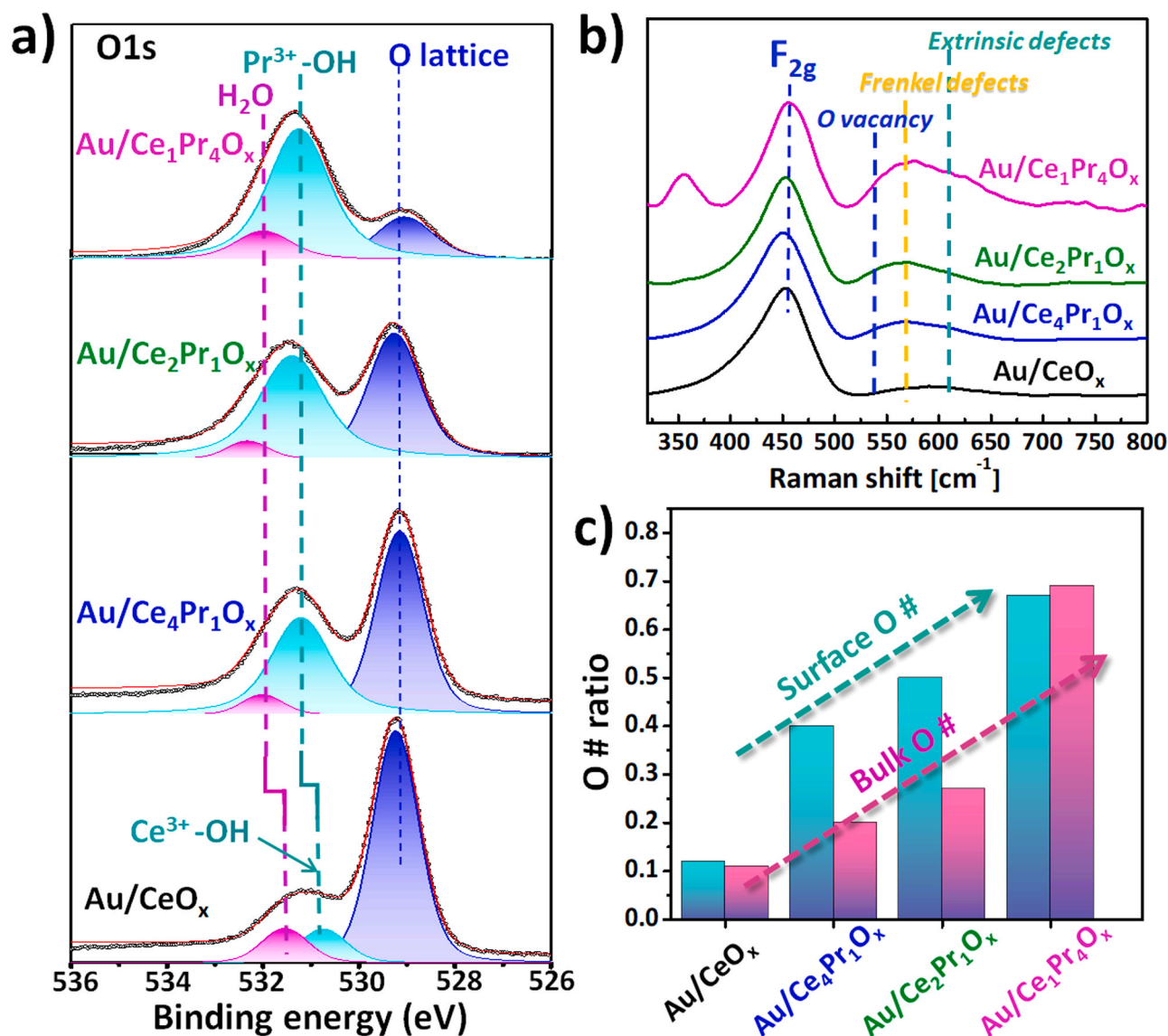
Fig. 5. a) Photoemission (XPS) O 1 s spectra of Au/Ce$_a$Pr$_b$O$_x$ catalysts (an O 1 s spectrum of Au/PrO$_x$ is shown in Fig. S6); b) Raman spectra of Au/Ce$_a$Pr$_b$O$_x$ and Au/CeO$_x$; c) bar graph of O vacancy ratios deduced from XPS and Raman (peak area of O vacancies/total peak areas). All samples were used in WGSR (2 vol% CO + 10 vol% H$_2$O/N$_2$, 10 h on-stream, 150–400°C).

oxygen vacancies (O #) is compared, and it can be seen that both increased with the praseodymium amount. Note that this merely shows ratios of peak areas related to vacancies and the total peak areas, but is not a quantification of the number of oxygen vacancies.

To further investigate the availability of such reactive oxygen species in Au/Ce$_a$Pr$_b$O$_x$, temperature programmed desorption of oxygen (O$_2$-TPD) and CO (CO-TPD) and temperature-programmed reduction (H$_2$-TPR) was applied. The O$_2$-TPD in Fig. 6a has two regions of desorption (dashed line). In the low-T region (50–225 °C) a peak at 110 °C can be assigned to adsorbed molecular oxygen (ad-O$_2$) on O vacancies. In the high-T region (225–800 °C), a broad peak is centered at 335 °C on Au/Ce$_4$Pr$_1$O$_x$, but shifts to higher temperature on Au/Ce$_2$Pr$_1$O$_x$ (380 °C) and Au/Ce$_1$Pr$_4$O$_x$ (411 °C), also increasing in intensity. The two sharp peaks on Au/Ce$_2$Pr$_1$O$_x$ (580 °C) and Au/Ce$_1$Pr$_4$O$_x$ (613 °C) can be attributed to a phase transformation of praseodymia (Pr$_x$O$_{2x-2}$ → Pr$_2$O$_3$) [36]. The high-T O$_2$ desorption peaks correspond to atomic (lattice) oxygen evolving from the oxide bulk and correlate with the stability of lattice O.

The relatively low desorption T of O$_2$ on Au/Ce$_4$Pr$_1$O$_x$ indicates the easy release of (surface) lattice O. Based on EXAFS and DFT studies by Dutta et al., it was proposed that substitution of Ce by other metal ion

(Ti) can create disorder, which then leads to an asymmetry in crystalline structure, resulting in the formation of weak, long M-O bonds [90]. Similarly, the distorted O lattice in Au/Ce$_4$Pr$_1$O$_x$ may lead to the formation of long Pr-O bonds, with O weakly bonded in the oxide, which would explain the easy oxygen release.

After CO exposure, the CO-TPD (mass 44) in Fig. 6b shows that only Au/Ce$_4$Pr$_1$O$_x$ has a CO$_2$ desorption peak at low temperature (165 °C), which indicates the adsorbed CO can easily react with surface O forming CO$_2$ (CO-TPD mass 28 in Fig. S7). The high temperature (> 400 °C) CO$_2$ desorption peaks on Au/Ce$_a$Pr$_b$O$_x$ can be attributed to the decomposition of carbonates created upon CO adsorption. In H$_2$-TPR, the hydrogen consumption in the range of 50–300 °C (Fig. 6c) can be assigned to the reduction of ionic Au (Au^{3+}, Au$^+$) and weakened Ce-O and Pr-O bonds adjacent to Au [65]. On Au/Ce$_4$Pr$_1$O$_x$ the reduction peak at around 110 °C is much more intense than those for Au/Ce$_2$Pr$_1$O$_x$ and Au/Ce$_1$-Pr$_4$O$_x$, once more indicating a high fraction of weakly bound surface O on Au/Ce$_4$Pr$_1$O$_x$, which can be easily removed by H$_2$. The results are in line with O$_2$-TPD and support the current hypothesis that Au/Ce$_4$Pr$_1$O$_x$ contains more active O, which may be adsorbed in the asymmetric oxygen vacancies and thus can be easily released, subsequently exposing

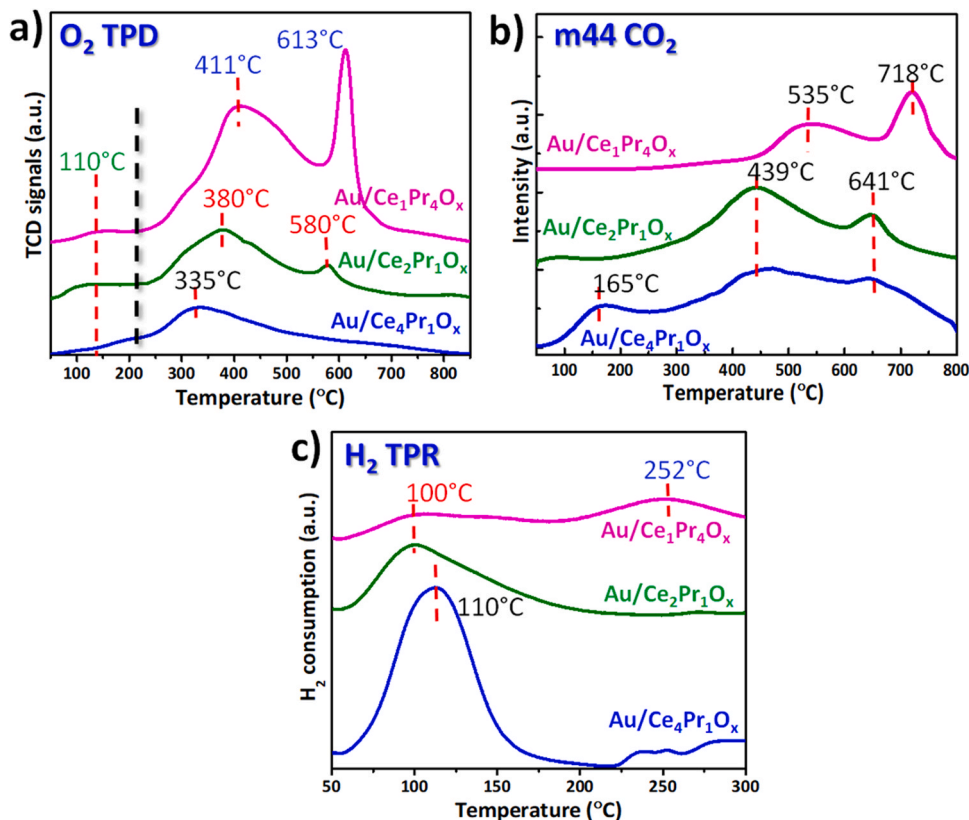**Fig. 6.** a) O_2-TPD, b) CO-TPD (showing m44) and c) H_2-TPR spectra of Au/$Ce_aPr_bO_x$ catalysts.

active O vacancy sites.

To further rationalize the experimental findings on doping effects, DFT calculations were carried out, first analyzing the dependence of the oxygen vacancy formation energy on the Pr content (Fig. 7a). We note that around a potential vacancy there are solely three metal sites within one layer, which may be replaced by Pr in stepwise fashion. These lateral variations should be the main source for asymmetry. The unit cell formally has the following composition $Ce_aPr_bO_x$, $a+b = 4$, $x = 8$. The vacancy formation energy for pure CeO_2 ($a=4$, $b=0$, $x = 8$) is calculated

at 2.3 eV, in line with previous studies reporting values from 2.1 to 2.5 eV depending on the location of the reducing electrons [81]. The vacancy formation energy drops notably when Pr is introduced into the system; to ~0 eV for $b = 1$, to 0.6 eV for $b = 2$, and to 0.7 eV for $b = 3$. For $b = 4$ we determined 0.5 eV, rationalizing the propensity for materials including Pr^{4+} to generally have more vacancies. Pure PrO_2 ($a=0$, $b=4$, $x = 8$) has three neighboring Pr atoms of the vacancy which is the same as for the system $Ce_1Pr_3O_8$. We note that the polarons from the vacancy formation were locating exclusively at Pr centers forming Pr^{3+}
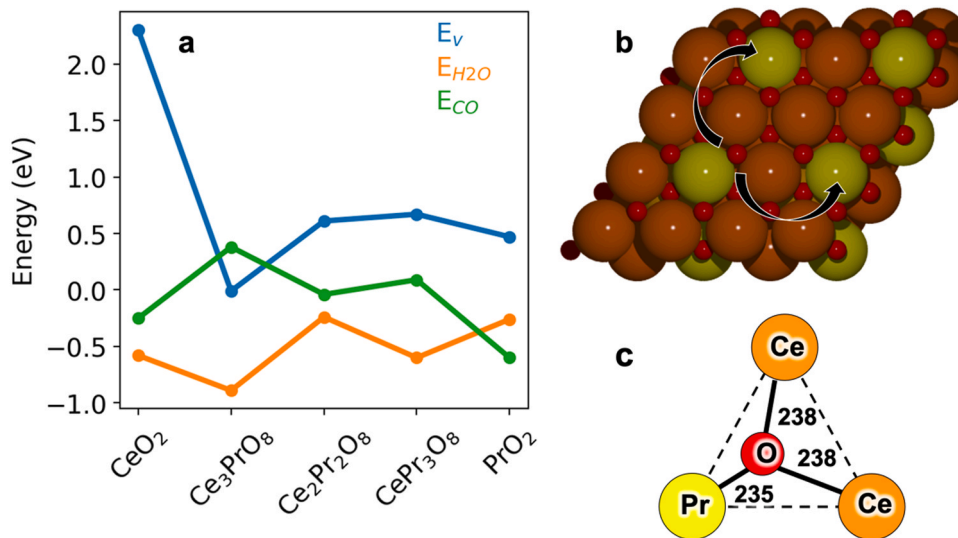

Fig. 7. a) DFT results for the vacancy formation energy E_v, adsorption energy of water at a vacancy site, E_{H2O}, as well as the CO adsorption energy at the metal site, E_{CO}; b) indication of centers accepting the reducing electrons after oxygen vacancy formation; c) asymmetric location of oxygen in the system Ce_3PrO_8 with the drawing being not to scale to better indicate the direction of the distortion.

(Fig. 7b). The standard electrochemical potential clearly favors the reduction of Pr^{4+} over that of Ce^{4+} to M^{3+} with 3.2 V vs 1.72 V, respectively [81]. This results in a limitation of the Pr extent that is favorable, as too much would hamper the Ce^{4+}/Ce^{3+} redox pair by exclusively locating electrons generated by the vacancy formation at praseodymium centers. Given that a catalytic cycle must be closed, the vacancy will have to be filled again with an oxygen atom. This is modeled by the adsorption of a water molecule at the vacancy site, which subsequently releases H_2 during WGS.
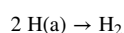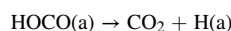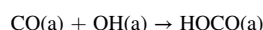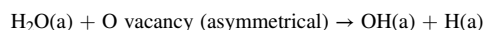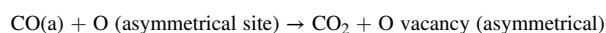
The binding energy of H_2O at the vacancy is computed at -0.6 eV (b = 0), -0.9 eV (b = 1), -0.2 eV (b = 2), -0.6 eV (b = 3), and -0.3 eV for PrO_2 (note that negative values indicate a favorable reaction). This again indicates that water binds most effective for a Ce-Pr system with ~25% Pr admixture, because the binding strength is again reduced when more Pr is incorporated. For E_v and E_{H2O} we thus determined an "inverted volcano plot" (Fig. 7a), with a slight admixture of Pr to the CeO_2 system showing the most favorable properties.

Interestingly, the Pr content also affects the coordination of the oxygen moiety forming the vacancy and its bond lengths to neighboring metal centers (Fig. 7c). For b = 1 the O–Pr bond of 235 pm is shorter than to the two O–Ce bonds of 238 pm and such an asymmetry was previously suggested as prerequisite for a catalytically active material. The asymmetry for b = 2 is hardly noticeable (both bonds to Pr being only 0.3 pm shorter than that to Ce), and for b = 0, 3, 4 there is no asymmetry at all. Altogether, this once more points to the system with Ce:Pr of 3:1 as most promising catalyst.

For completeness, the CO binding energies at the support were calculated as well, although CO is generally considered to be adsorbed on the gold clusters. For b = 0 it is -0.3 eV at Ce. For b = 1, when CO sits at Pr, an energy of 0.4 eV was determined. For b = 2, the CO binding energy at Pr is ~0 eV. At b = 3, the CO binding energy amounts to 0.1 eV at Pr. For PrO_2, the CO binding energy is again favorable with -0.6 eV. Nevertheless, for the most active support (b = 1), CO binds weakest, so that adsorption on Au sites is strongly preferred, in agreement with the general expectation (Fig. 8).

Altogether, the combined experimental and theoretical results rationalize why Au/Ce_4Pr_1Ox shows the highest catalytic activity, although it does not have the highest oxygen vacancy ratio among the $Au/Ce_aPr_bO_x$ catalyst, neither on the surface nor in the bulk. Our results are also in line with previous related studies. Zhou, Lee, and Reddy et al. found similar trends on $Ce_{1-x}Bi_xO_{2-\delta}$, $Ce_{1-x}Mn_xO_{2-\delta}$ and $Ce_{1-x}La_xO_{2-\delta}$ catalyst, respectively [12,13,91]. While atomic ratios of Ce:Bi, Ce:Mn and Ce:La around 4:1 led to the highest activity in the redox reaction (aerobic oxidation of 5-hydroxymethyl-2-furfural and CO oxidation), higher doping ratios resulted in an increased oxygen vacancy concentration, but at the expense of decreasing activity. Zhou et al. attributed this to the changing chemical environment of the oxygen vacancies, as

the substitution of Ce by other trivalent cations would generate "asymmetric oxygen vacancies". Similar to $Ce_{0.8}Bi_{0.2}O_{2-\delta}$, when in our case an octacoordinated Ce^{4+} is replaced by a hexacoordinated Pr^{3+} asymmetrical oxygen vacancies, Pr-□(-Ce)₃, are created. These asymmetrical oxygen vacancies prefer to be filled by adsorbed oxygen species, due to local charge balance and to obtain a stable coordination of Ce^{4+}. The oxygen in these sites is also easily released due to the asymmetric bonding. In WGSR, CO will react with the active O creating the exposed asymmetrical oxygen vacancies, and to re-fill these oxygen vacancies, water will be adsorbed and dissociated to OH and H [92]. The generated OH groups can then react with CO, eventually yielding CO_2 and H_2, the final products of WGSR. The entire pathway is summarized below:

CO(a) + O (asymmetrical site) → CO_2 + O vacancy (asymmetrical)

H_2O(a) + O vacancy (asymmetrical) → OH(a) + H(a)

CO(a) + OH(a) → HOCO(a)

HOCO(a) → CO_2 + H(a)

2 H(a) → H_2

With a Ce:M (M: metal) around 4:1, the number of "asymmetric oxygen vacancies" should be the highest, but by increasing the M-doping, M-rich clusters will form, following a "similarity and inter-miscibility" tendency in solid solutions [13,91]. The number of asymmetric oxygen vacancies may be affected by Pr-rich clusters. For low concentrations, Pr cations are separated in the fluorite structure, i.e. no Pr-O-Pr is formed, but when the Pr loading ratio increases, these types of bonds will occur. These M-rich clusters will strongly reduce the adsorption capability of the oxygen vacancies. Therefore, further doping will not enhance but hinder the reaction, explaining why an increased oxygen vacancy number does not increase the reaction rate.

4. Conclusions

Solid solutions of rod-shaped ceria-praseodymia oxide with different mixing ratios were successfully synthesized via a hydrothermal method. By varying the content of Pr in the mixed oxides, the environment of lattice oxygen could be tuned, resulting in the creation of very specific lattice oxygen of asymmetric symmetry, i.e., with Pr-O bonds shorter than the Ce-O bonds, that leads to facile vacancy formation. Their highest relative abundance in $Au/Ce_4Pr_1O_x$ led to the highest activity of all catalysts tested (TOF 2.0 s^{-1} at 360 °C with long-term stability). The $Ce_4Pr_1O_x$ support also exhibited the highest O mobility and availability. The optimum extent of Pr around 25% was rationalized by DFT calculations, based on the lowest oxygen vacancy formation energy and the highest H_2O binding energy. DFT calculations also revealed the
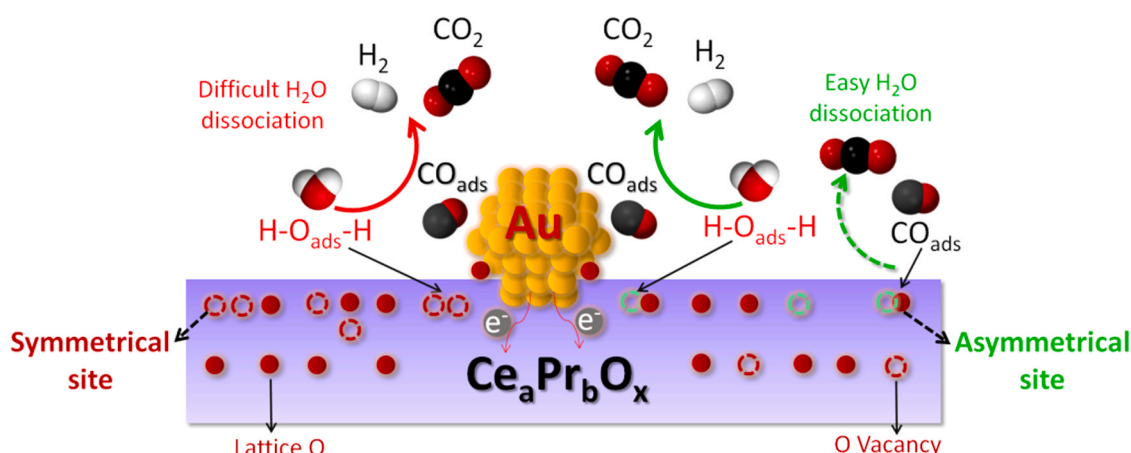

Fig. 8. Schematic illustration of the H_2O dissociation on the asymmetrical O vacancy site and the following steps for WGSR.

asymmetry of the active vacancy site in the most active catalyst. However, further increasing the amount of Pr doping, and thus the number of both surface and bulk oxygen vacancies, did not increase the catalytic activity of $Au/Ce_aPr_bO_x$ as the asymmetry vanished, with oxygen now nearly exclusively surrounded by Pr centers. This proved that the nature of the vacancy sites plays a more important role in influencing the catalytic activity than just their mere abundance.

The current study highlights a promising route for designing and modifying the active sites in mixed oxide catalysts, advancing from vacancy numbers to vacancy types. This concept can also be extended to other metal/mixed oxide heterogeneous catalytic systems.

CRediT authorship contribution statement

J. Shi designed and supervised the project, drafted the manuscript, analyzed the data and prepared the graphs. H.L. Li, T. Wang and W. X. Zhao prepared and tested the catalysts. H.L. Li and T. Wang performed the XRD and Raman characterization, W. X. Zhao performed O_2-TPD, CO-TPD, H_2-TPR. A. Genest carried out the DFT calculations of structures and adsorption properties. P.F. Qi helped modify the manuscript. G. Rupprechter was deeply involved in the data interpretation and in finalizing the manuscript.

Declaration of Competing Interest

The authors declare that they have no known competing financial interests or personal relationships that could have appeared to influence the work reported in this paper.

Acknowledgement

Appendix A. Supporting information

Supplementary data associated with this article can be found in the online version at doi:10.1016/j.apcatb.2021.120789.

References

[1] I.E. Wachs, K. Routray, Catalysis science of bulk mixed oxides, ACS Catal. 2 (2012) 1235–1246.
[2] D.J. Stacchiola, S.D. Senanayake, P. Liu, J.A. Rodriguez, Fundamental studies of well-defined surfaces of mixed-metal oxides: special properties of MO(x)/TiO2 (110) {M = V, Ru, Ce, or W}, Chem. Rev. 113 (2013) 4373–4390.
[3] U. Diebold, G. Rupprechter, Preface: surface science of functional oxides, Surf. Sci. 681 (2019) A1.
[4] L. Lukashuk, K. Föttinger, E. Kolar, C. Rameshan, D. Teschner, M. Hävecker, A. Knop-Gericke, N. Yigit, H. Li, E. McDermott, M. Stöger-Pollach, G. Rupprechter, Operando XAS and NAP-XPS studies of preferential CO oxidation on Co3O4 and CeO2-Co3O4 catalysts, J. Catal. 344 (2016) 1–15.
[5] J. Yang, L. Lukashuk, J. Akbarzadeh, M. Stöger-Pollach, H. Peterlik, K. Föttinger, G. Rupprechter, U. Schubert, Different synthesis protocols for Co3O4 -CeO2 catalysts–part 1: influence on the morphology on the nanoscale, Chem. Eur. J. 21 (2015) 885–892.
[6] J.G. Joon, B. Park, J. Evans, D. Stacchiola, S. Ma, P. Liu, A. Nambu, J. Fernandez Sanz, J. Hrbeka, J.A. Rodriguez, High catalytic activity of Au/CeOx/TiO2(110) controlled by the nature of the mixed-metal oxide at the nanometer level, PNAS 106 (2009) 4975–4980.
[7] J. Yang, N. Yigit, J. Möller, G. Rupprechter, Co3O4 -CeO2 nanocomposites for low-temperature CO oxidation, Chem. Eur. J. 27 (2021) 1–10.
[8] R. Si, J. Tao, J. Evans, J.B. Park, L. Barrio, J.C. Hanson, Y. Zhu, J. Hrbek, J. A. Rodriguez, Effect of ceria on gold–titania catalysts for the water–gas shift reaction: fundamental studies for Au/CeOx/TiO2(110) and Au/CeOx/TiO2 Powders, J. Phys. Chem. C 116 (2012) 23547–23555.
[9] I. Ro, J. Resasco, P. Christopher, Approaches for understanding and controlling interfacial effects in oxide-supported metal catalysts, ACS Catal. 8 (2018) 7368–7387.
[10] E.W. McFarland, H. Metiu, Catalysis by doped oxides, Chem. Rev. 113 (2013) 4391–4427.
[11] J. Paier, C. Penschke, J. Sauer, Oxygen defects and surface chemistry of ceria: quantum chemical studies compared to experiment, Chem. Rev. 113 (2013) 3949–3985.
[12] K.J. Lee, J.H. Lee, S. Jeoung, H.R. Moon, Transformation of metal-organic frameworks/coordination polymers into functional nanostructured materials: experimental approaches based on mechanistic insights, Acc. Chem. Res. 50 (2017) 2684–2692.
[13] K. Yu, L.L. Lou, S. Liu, W. Zhou, Asymmetric oxygen vacancies: the intrinsic redox active sites in metal oxide catalysts, Adv. Sci. 7 (2020), 1901970.
[14] S.R. Spurgeon, T.C. Kaspar, V. Shutthanandan, J. Gigax, L. Shao, M. Sassi, Asymmetric lattice disorder induced at oxide interfaces, Adv. Mater. Interfaces 7 (2020), 1901944.
[15] X. Zhang, C. Pei, X. Chang, S. Chen, R. Liu, Z.J. Zhao, R. Mu, J. Gong, FeO6 octahedral distortion activates lattice oxygen in perovskite ferrite for methane partial oxidation coupled with CO2 Splitting, J. Am. Chem. Soc. 142 (2020) 11540–11549.
[16] F. Esch, L. Zhou, T. Montini, P. Fornasiero, G. Comelli, R. Rosei, S. Fabris, C. Africh, Electron localization determines defect formation on ceria substrates, Science 309 (2005) 752–755.
[17] X. Han, N. Amrane, Z. Zhang, M. Benkraouda, Unraveling the negative role of oxygen-vacancy cluster in ionic conductivity in CeO2: hybrid functional study, J. Phys. Chem. C 122 (2018) 5871–5880.
[18] M. Sankar, Q. He, R.V. Engel, M.A. Sainna, A.J. Logsdail, A. Roldan, D.J. Willock, N. Agarwal, C.J. Kiely, G.J. Hutchings, Role of the support in gold-containing nanoparticles as heterogeneous catalysts, Chem. Rev. 120 (2020) 3890–3938.
[19] J. Zhang, H. Wang, L. Wang, S. Ali, C. Wang, L. Wang, X. Meng, B. Li, D.S. Su, F. S. Xiao, Wet-chemistry strong metal-support interactions in titania-supported Au catalysts, J. Am. Chem. Soc. 141 (2019) 2975–2983.
[20] L. Wang, J. Zhang, Y. Zhu, S. Xu, C. Wang, C. Bian, X. Meng, F.-S. Xiao, Strong metal–support interactions achieved by hydroxide-to-oxide support transformation for preparation of sinter-resistant gold nanoparticle catalysts, ACS Catal. 7 (2017) 7461–7465.
[21] A. Bruix, J.A. Rodriguez, P.J. Ramirez, S.D. Senanayake, J. Evans, J.B. Park, D. Stacchiola, P. Liu, J. Hrbek, F. Illas, A new type of strong metal-support interaction and the production of H2 through the transformation of water on Pt/CeO2(111) and Pt/CeO(x)/TiO2(110) catalysts, J. Am. Chem. Soc. 134 (2012) 8968–8974.
[22] Q. Xiao, Y. Wang, Z.-J. Zhao, C. Pei, S. Chen, L. Gao, R. Mu, Q. Fu, J. Gong, Defect-mediated reactivity of Pt/TiO2 catalysts: the different role of titanium and oxygen vacancies, Sci. China Chem. 63 (9) (2020).
[23] C. Doornkamp, V. Ponec, The universal character of the Mars and Van Krevelen mechanism, J. Mol. Catal. A Chem. 162 (2000) 19–32.
[24] D. Widmann, R.J. Behm, Dynamic surface composition in a Mars-van Krevelen type reaction: CO oxidation on Au/TiO2, J. Catal. 357 (2018) 263–273.
[25] K. Hayek, B. Klötzer, W. Reichl, G. Rupprechter, Studies of metal–support interactions with "real" and "inverted" model systems: reactions of CO and small hydrocarbons with hydrogen on noble metals in contact with oxides, Top. Catal. 13 (2000) 55–66.
[26] M. Cargnello, V.V.T. Doan-Nguyen, T.R. Gordon, R.E. Diaz, E.A. Stach, R.J. Gorte, P. Fornasiero, C.B. Murray, Control of metal nanocrystal size reveals metal-support interface role for ceria catalysts, Science (2013) 771–773.
[27] G. Li, G.R. Blake, T.T. Palstra, Vacancies in functional materials for clean energy storage and harvesting: the perfect imperfection, Chem. Soc. Rev. 46 (2017) 1693–1706.
[28] A. Trovarelli, J. Llorca, Ceria catalysts at nanoscale: how do crystal shapes shape catalysis? ACS Catal. 7 (2017) 4716–4735.
[29] T. Montini, M. Melchionna, M. Monai, P. Fornasiero, Fundamentals and catalytic applications of CeO2-based materials, Chem. Rev. 116 (2016) 5987–6041.
[30] Y. Suchorski, S.M. Kozlov, I. Bespalov, M. Datler, D. Vogel, Z. Budinska, M. Neyman, G. Rupprechter, The role of metal/oxide interfaces for long-range metal particle activation during CO oxidation, Nat. Mater. 17 (2018) 519–522.
[31] N. Liu, M. Xu, Y. Yang, S. Zhang, J. Zhang, W. Wang, L. Zheng, S. Hong, M. Wei, Auδ−–Ov–Ti3+ interfacial site: catalytic active center toward low-temperature water gas shift reaction, ACS Catal. 9 (2019) 2707–2717.
[32] M. Xu, S. Yao, D. Rao, Y. Niu, N. Liu, M. Peng, P. Zhai, Y. Man, L. Zheng, B. Wang, B. Zhang, D. Ma, M. Wei, Insights into interfacial synergistic catalysis over Ni@TiO2- x catalyst toward water-gas shift reaction, J. Am. Chem. Soc. 140 (2018) 11241–11251.
[33] J. Shi, A. Wittstock, C. Mahr, M.M. Murshed, T.M. Gesing, A. Rosenauer, M. Bäumer, Nanoporous gold functionalized with praseodymia-titania mixed oxides as a stable catalyst for the water-gas shift reaction, Phys. Chem. Chem. Phys. 21 (2019) 3278–3286.
[34] J. Shi, H. Li, W. Zhao, P. Qi, H. Wang, Praseodymium hydroxide/gold-supported precursor: a new strategy for preparing stable and active catalyst for the water-gas shift reaction, Catal. Sci. Technol. 10 (2020) 7291–7301.
[35] G. Niu, M.H. Zoellner, T. Schroeder, A. Schaefer, J.H. Jhang, V. Zielasek, M. Bäumer, H. Wilkens, J. Wollschlager, R. Olbrich, C. Lammers, M. Reichling,

Controlling the physics and chemistry of binary and ternary praseodymium and cerium oxide systems, Phys. Chem. Chem. Phys. 17 (2015) 24513–24540.

[36] P. Sonström, J. Birkenstock, Y. Borchert, L. Schilinsky, P. Behrend, K. Gries, K. Müller, A. Rosenauer, M. Bäumer, Nanostructured praseodymium oxide: correlation between phase transitions and catalytic activity, ChemCatChem 2 (2010) 694–704.

[37] Z. Zhang, Y. Wang, J. Lu, C. Zhang, M. Wang, M. Li, X. Liu, F. Wang, Conversion of isobutene and formaldehyde to diol using praseodymium-doped CeO2 catalyst, ACS Catal. 6 (2016) 8248–8254.

[38] Z. Zhang, Y. Wang, J. Lu, J. Zhang, M. Li, X. Liu, F. Wang, Pr-doped CeO2 catalyst in the prins condensation–hydrolysis reaction: are all of the defect sites catalytically active? ACS Catal. 8 (2018) 2635–2644.

[39] B. Zhou, K. Xi, L.-J. Fan, Y. Zhou, Y. Wang, Q.-L. Zhu, H.-F. Lu, A comparative study on Ce–Pr and Ce–Mn mixed oxide catalysts toward soot catalytic combustion, Appl. Catal. A: Gen. 562 (2018) 1–10.

[40] M. Guo, X. Liu, A. Amorelli, Activation of small molecules over praseodymium-doped ceria, Chin. J. Catal. 40 (2019) 1800–1809.

[41] K. Harada, T. Oishi, S. Hamamoto, T. Ishihara, Lattice oxygen activity in Pr- and La-Doped CeO2 for low-temperature soot oxidation, J. Phys. Chem. C 118 (2013) 559–568.

[42] L. Fan, K. Xi, Y. Zhou, Q. Zhu, Y. Chen, H. Lu, Design structure for CePr mixed oxide catalysts in soot combustion, RSC Adv. 7 (2017) 20309–20319.

[43] J.C. Martínez-Munuera, M. Zoccoli, J. Giménez-Mañogil, A. García-García, Lattice oxygen activity in ceria-praseodymia mixed oxides for soot oxidation in catalysed gasoline particle filters, Appl. Catal. B Environ. 245 (2019) 706–720.

[44] E.J. Jeong, J.H. Lee, S.H. Lee, C.S. Park, J.W. Choung, C.H. Kim, K.Y. Lee, Cee.ngd Catalysis B: environmental raseodymia mixed oxides for soot oxidation in cataly, ChemCatChem 11 (2019) 2131–2141.

[45] X.P. Fu, L.W. Guo, W.W. Wang, C. Ma, C.J. Jia, K. Wu, R. Si, L.D. Sun, C.H. Yan, Direct identification of active surface species for the water-gas shift reaction on a gold-ceria catalyst, J. Am. Chem. Soc. 141 (2019) 4613–4623.

[46] J.A. Rodriguez, P. Liu, J. Hrbek, J. Evans, M. Perez, Water gas shift reaction on Cu and Au nanoparticles supported on CeO2(111) and ZnO(0001): intrinsic activity and importance of support interactions, Angew. Chem. Int. Ed. Engl. 46 (2007) 1329–1332.

[47] Q. Fu, H. Saltsburg, M. Flytzani-Stephanopoulos, Active nonmetallic Au and Pt species on ceria-based water-gas shift catalysts, Science 301 (2003) 935–938.

[48] X. Zhang, M. Zhang, Y. Deng, M. Xu, L. Artiglia, W. Wen, R. Gao, B. Chen, S. Yao, X. Zhang, M. Peng, J. Yan, A. Li, Z. Jiang, X. Gao, S. Cao, C. Yang, A.J. Kropf, J. Shi, J. Xie, M. Bi, J.A. van Bokhoven, Y.W. Li, X. Wen, M. Flytzani-Stephanopoulos, C. Shi, W. Zhou, D. Ma, A stable low-temperature H2-production catalyst by crowding Pt on alpha-MoC, Nature 589 (2021) 396–401.

[49] J.A. Rodriguez, S. Ma, P. Liu, J. Hrbek, J. Evans, M. Pérez, Activity of CeOx and TiOx nanoparticles grown on Au(111) in the water-gas shift reaction, Science 318 (2007) 1757–1759.

[50] J. Shi, A. Schaefer, A. Wichmann, M.M. Murshed, T.M. Gesing, A. Wittstock, M. Bäumer, Nanoporous gold-supported ceria for the water–gas shift reaction: UHV inspired design for applied catalysis, J. Phys. Chem. C 118 (2014) 29270–29277.

[51] J. Shi, C. Mahr, M.M. Murshed, V. Zielasek, A. Rosenauer, T.M. Gesing, M. Bäumer, A. Wittstock, A versatile sol–gel coating for mixed oxides on nanoporous gold and their application in the water gas shift reaction, Catal. Sci. Technol. 6 (2016) 5311–5319.

[52] J. Shi, C. Mahr, M.M. Murshed, T.M. Gesing, A. Rosenauer, M. Bäumer, A. Wittstock, Steam reforming of methanol over oxide decorated nanoporous gold catalysts: a combined in situ FTIR and flow reactor study, Phys. Chem. Chem. Phys. 19 (2017) 8880–8888.

[53] L. Kępiński, J. Okal, Occurrence and mechanism of formation of CeOCl in Pd/CeO2 catalysts, J. Catal. 192 (2000) 48–53.

[54] H.S. Oh, J.H. Yang, C.K. Costello, Y.M. Wang, S.R. Bare, H.H. Kung, M.C. Kung, Selective catalytic oxidation of CO: effect of chloride on supported Au catalysts, J. Catal. 210 (2002) 375–386.

[55] N. Barrabes, K. Föttinger, J. Llorca, A. Dafinov, F. Medina, J. Sa, C. Hardacre, G. Rupprechter, Pretreatment effect on Pt/CeO2 catalyst in the selective hydrodechlorination of trichloroethylene, J. Phys. Chem. C 114 (2010) 17675–17682.

[56] A. Taketoshi, T. Ishida, H. Ohashi, T. Honma, M. Haruta, Preparation of gold clusters on metal oxides by deposition-precipitation with microwave drying and their catalytic performance for CO and sulfide oxidation, Chin. J. Catal. 38 (2017) 1888–1898.

[57] K.B. John, P. Perdew, Matthias ernzerhof, generalized gradient approximation made simple, Phys. Rev. Lett. 77 (1996) 3865–3868.

[58] G. Kresse, J. Furthmüller, Efficient iterative schemes for ab initio total-energy calculations using a plane-wave basis set, Phys. Rev. B 54 (1996) 11169–11186.

[59] G. Kresse, J. Furthmüller, Efficiency of ab-initio total energy calculations for metals and semiconductors using a plane-wave basis set, Comput. Mater. Sci. 6 (1996) 15–50.

[60] P.E. Blöchl, C.J. Först, J Schimpl, Projector augmented wave method: ab initio molecular dynamics with full wave functions, Bull. Mater. Sci. 26 (2003) 33–41.

[61] P.E. Blöchl, Projector augmented-wave method, Phys. Rev. B Condens. Matter 50 (1994) 17953–17979.

[62] P.X. Huang, F. Wu, B.L. Zhu, G.R. Li, Y.L. Wang, X.P. Gao, H.Y. Zhu, T.Y. Yan, W. P. Huang, S.M. Zhang, D.Y. Song, Praseodymium hydroxide and oxide nanorods and Au/Pr6O11 nanorod catalysts for CO oxidation, J. Phys. Chem. B 110 (2006) 1614–1620.

[63] C. Dong, Y. Zhou, N. Ta, W. Shen, Formation mechanism and size control of ceria nanocubes, CrystEngComm 22 (2020) 3033–3041.

[64] A. Wolfbeisser, O. Sophiphun, J. Bernardi, J. Wittayakun, K. Föttinger, G. Rupprechter, Methane dry reforming over ceria-zirconia supported Ni catalysts, Catal. Today 277 (2016) 234–245.

[65] R. Si, M. Flytzani-Stephanopoulos, Shape and crystal-plane effects of nanoscale ceria on the activity of Au-CeO2 catalysts for the water-gas shift reaction, Angew. Chem. Int Ed. Engl. 47 (2008) 2884–2887.

[66] D. Matthey, J.G. Wang, S. Wendt, J. Matthiesen, R. Schaub, E. Lægsgaard, B. Hammer, F. Besenbacher, Enhanced bonding of gold nanoparticles on oxidized TiO2(110), Science 315 (2007) 1692–1696.

[67] M.A. Brown, Y. Fujimori, F. Ringleb, X. Shao, F. Stavale, N. Nilius, M. Sterrer, H.-J. Freund, Oxidation of Au by surface OH: nucleation and electronic structure of gold on hydroxylated MgO(001), J. Am. Chem. Soc. 133 (2011) 10668–10676.

[68] S. Penner, G. Rupprechter, H. Sauer, D.S. Su, R. Tessadri, R. Podloucky, R. Schlögl, K. Hayek, Pt/ceria thin film model catalysts after high-temperature reduction: a (HR)TEM study, Vacuum 71 (2003) 71–76.

[69] N. Ta, J.J. Liu, S. Chenna, P.A. Crozier, Y. Li, A. Chen, W. Shen, Stabilized gold nanoparticles on ceria nanorods by strong interfacial anchoring, J. Am. Chem. Soc. 134 (2012) 20585–20588.

[70] W. Chen, L. Sun, B. Kozinsky, C.M. Friend, E. Kaxiras, P. Sautet, R.J. Madix, Effect of frustrated rotations on the pre-exponential factor for unimolecular reactions on surfaces: a case study of alkoxy dehydrogenation, J. Phys. Chem. C 124 (2019) 1429–1437.

[71] J.E.S. van der Hoeven, H.T. Ngan, A. Taylor, N.M. Eagan, J. Aizenberg, P. Sautet, R. J. Madix, C.M. Friend, Entropic control of HD exchange rates over dilute Pd-in-Au alloy nanoparticle catalysts, ACS Catal. 11 (2021) 6971–6981.

[72] W. Deng, M. Flytzani-Stephanopoulos, On the issue of the deactivation of Au-ceria and Pt-ceria water-gas shift catalysts in practical fuel-cell applications, Angew. Chem. Int. Ed. Engl. 45 (2006) 2285–2289.

[73] H. Yan, C. Yang, W.P. Shao, L.H. Cai, W.W. Wang, Z. Jin, C.J. Jia, Construction of stabilized bulk-nano interfaces for highly promoted inverse CeO2/Cu catalyst, Nat. Commun. 10 (2019) 3470.

[74] X. Cai, W. Hu, S. Xu, D. Yang, M. Chen, M. Shu, R. Si, W. Ding, Y. Zhu, Structural relaxation enabled by internal vacancy available in a 24-atom gold cluster reinforces catalytic reactivity, J. Am. Chem. Soc. 142 (2020) 4141–4153.

[75] W. Deng, A.I. Frenkel, R. Si, M. Flytzani-Stephanopoulos, Reaction-relevant gold structures in the low temperature water-gas shift reaction on Au-CeO2, J. Phys. Chem. C. 112 (2008) 12834–12840.

[76] A.Y. Klyushin, T.C. Rocha, M. Hävecker, A. Knop-Gericke, R. Schlögl, A near ambient pressure XPS study of Au oxidation, Phys. Chem. Chem. Phys. 16 (2014) 7881–7886.

[77] M. Schmid, R.J. Madix, C.M. Friend, The creation of microscopic surface structures by interfacial diffusion of Au and Ag on Ag(110): a XPS and STM study, Surf. Sci. 643 (2016) 36–44.

[78] A. Schaefer, S. Gevers, V. Zielasek, T. Schroeder, J. Falta, J. Wollschlager, M. Bäumer, Photoemission study of praseodymia in its highest oxidation state: the necessity of in situ plasma treatment, J. Chem. Phys. 134 (2011), 054701.

[79] H. Wilkens, S. Gevers, S. Röhe, A. Schaefer, M. Bäumer, M.H. Zoellner, T. Schroeder, J. Wollschläger, Structural changes of ultrathin Cub-PrO2(111)/Si (111) films due to thermally induced oxygen desorption, J. Phys. Chem. C. 118 (2014) 3056–3061.

[80] M.H. Zoellner, G. Niu, J.-H. Jhang, A. Schaefer, P. Zaumseil, M. Bäumer, T. Schroeder, Temperature-dependent reduction of epitaxial Ce1−xPrxO2−δ(x= 0–1) thin films on Si(111): a combined temperature-programmed desorption, X-ray diffraction, X-ray photoelectron spectroscopy, and raman study, J. Phys. Chem. C 117 (2013) 24851–24857.

[81] D.R. Lide, G. Baysinger, L.I. Berger, R.N. Goldberg, H.V. Kehiaian, K. Kuchitsu, G. Rosenblatt, D.L. Roth, D. Zwillinger. CRC Handbook of Chemistry and Physics, CRC Press, Boca Raton, 2005, pp. 23–26.

[82] C. Schilling, A. Hofmann, C. Hess, M.V. Ganduglia-Pirovano, Raman spectra of polycrystalline CeO2: a density functional theory study, J. Phys. Chem. C. 121 (2017) 20834–20849.

[83] C. Schilling, C. Hess, Real-time observation of the defect dynamics in working Au/CeO2 catalysts by combined operando raman/UV–Vis spectroscopy, J. Phys. Chem. C. 122 (2018) 2909–2917.

[84] Y. Xu, F. Wang, X. Liu, Y. Liu, M. Luo, B. Teng, M. Fan, X. Liu, Resolving a decade-long question of oxygen defects in raman spectra of ceria-based catalysts at atomic level, J. Phys. Chem. C 123 (2019) 18889–18894.

[85] H. Sohn, G. Celik, S. Gunduz, D. Dogu, S. Zhang, J. Shan, F.F. Tao, U.S. Ozkan, Oxygen mobility in pre-reduced nano- and macro-ceria with co loading: an AP-XPS, in-Situ DRIFTS and TPR study, Catal. Lett. 147 (2017) 2863–2876.

[86] C. Wen, Y. Zhu, Y.C. Ye, S.R. Zhang, F. Cheng, Y. Liu, P. Wang, F.F. Tao, Water gas shift reaction on metal nanoclusters encapsulated in mesoporous ceria studied with ambient-pressure X-ray photoelectron spectroscopy, ACS Nano 6 (2012) 9305–9313.

[87] Z. Liu, T. Duchon, H. Wang, D.C. Grinter, I. Waluyo, J. Zhou, Q. Liu, B. Jeong, E. J. Crumlin, V. Matolin, D.J. Stacchiola, J.A. Rodriguez, S.D. Senanayake, Ambient pressure XPS and IRRAS investigation of ethanol steam reforming on Ni-CeO2(111) catalysts: an in situ study of C-C and O-H bond scission, Phys. Chem. Chem. Phys. 18 (2016) 16621–16628.

[88] Y. Lee, G. He, A.J. Akey, R. Si, M. Flytzani-Stephanopoulos, I.P. Herman, Raman analysis of mode softening in nanoparticle CeO(2-delta) and Au-CeO(2-delta) during CO oxidation, J. Am. Chem. Soc. 133 (2011) 12952–12955.

[89] E. Sartoretti, C. Novara, F. Giorgis, M. Piumetti, S. Bensaid, N. Russo, D. Fino, In situ Raman analyses of the soot oxidation reaction over nanostructured ceria-based catalysts, Sci. Rep. 9 (2019) 3875.

[90] G. Dutta, U.V. Waghmare, T. Baidya, M.S. Hegde, K.R. Priolkar, P.R. Sarode, Origin of enhanced reducibility/oxygen storage capacity of Ce1-xTixO2 compared to CeO2 or TiO2, Chem. Mater. 18 (2006) 3249–3256.

[91] K. Yu, D. Lei, Y. Feng, H. Yu, Y. Chang, Y. Wang, Y. Liu, G.-C. Wang, L.-L. Lou, S. Liu, W. Zhou, The role of Bi-doping in promoting electron transfer and catalytic performance of Pt/3DOM-Ce1−Bi O2−δ, J. Catal. 365 (2018) 292–302.

[92] P. Ebrahimi, A. Kumar, M. Khraisheh, A review of recent advances in water-gas shift catalysis for hydrogen production, Emergent Mater. 3 (2020) 881–917.